

# X-ray analysis methods for sources from self-modulated laser wakefield acceleration driven by picosecond lasers

Cite as: Rev. Sci. Instrum. **90**, 033503 (2019); <https://doi.org/10.1063/1.5082965>  
 Submitted: 26 November 2018 . Accepted: 20 February 2019 . Published Online: 12 March 2019

P. M. King , N. Lemos , J. L. Shaw, A. L. Milder, K. A. Marsh, A. Pak, B. M. Hegelich , P. Michel, J. Moody, C. Joshi, and F. Albert



View Online



Export Citation



CrossMark

## ARTICLES YOU MAY BE INTERESTED IN

[Transparent high-pressure nozzles for visualization of nozzle internal and external flow phenomena](#)

Review of Scientific Instruments **90**, 033702 (2019); <https://doi.org/10.1063/1.5065658>

[Measurement of the injecting time of picosecond laser in indirect-drive integrated fast ignition experiments using an x-ray streak camera](#)

Review of Scientific Instruments **90**, 033504 (2019); <https://doi.org/10.1063/1.5050039>

[Betatron x-ray radiation from laser-plasma accelerators driven by femtosecond and picosecond laser systems](#)

Physics of Plasmas **25**, 056706 (2018); <https://doi.org/10.1063/1.5020997>

## Lock-in Amplifiers up to 600 MHz

starting at

\$6,210



 Zurich Instruments

Watch the Video 



# X-ray analysis methods for sources from self-modulated laser wakefield acceleration driven by picosecond lasers

Cite as: Rev. Sci. Instrum. 90, 033503 (2019); doi: 10.1063/1.5082965

Submitted: 26 November 2018 • Accepted: 20 February 2019 •

Published Online: 12 March 2019



P. M. King,<sup>1,2,a</sup>  N. Lemos,<sup>1</sup>  J. L. Shaw,<sup>3</sup> A. L. Milder,<sup>3</sup> K. A. Marsh,<sup>4</sup> A. Pak,<sup>1</sup> B. M. Hegelich,<sup>2,5,6</sup>  P. Michel,<sup>1</sup> J. Moody,<sup>1</sup> C. Joshi,<sup>4</sup> and F. Albert<sup>1</sup>

## AFFILIATIONS

<sup>1</sup>NIF and Photon Sciences, Lawrence Livermore National Laboratory, Livermore, California 94550, USA

<sup>2</sup>Department of Physics, University of Texas at Austin, Austin, Texas 78712, USA

<sup>3</sup>Laboratory for Laser Energetics, University of Rochester, Rochester, New York 14623, USA

<sup>4</sup>Department of Electrical Engineering, University of California Los Angeles, Los Angeles, California 90095, USA

<sup>5</sup>Center for Relativistic Laser Science, Institute for Basic Science, Gwangju 61005, South Korea

<sup>6</sup>Department of Physics and Photon Science, GIST, Gwangju 61005, South Korea

<sup>a</sup>king100@llnl.gov

## ABSTRACT

A versatile set of methods for analyzing x-ray energy spectra and photon flux has been developed for laser plasma accelerator experiments driven by picosecond lasers. Forward fit provides extrapolated broad energy spectrum measurements, while Ross pair and differential average transmission analysis provide directly measured data points using a particular diagnostic. Combining these methods allows the measurement of x-ray energy spectra with improved confidence. We apply the methods to three diagnostics (filter wheel, stacked image plate spectrometer, and step wedge), each sensitive to a different region of x-ray energies (<40 keV, 35–100 keV, and 60–1000 keV, respectively), to characterize the analysis methods using laser-driven bremsstrahlung x-rays. We then apply the methods to measure three x-ray mechanisms, betatron, inverse Compton scattering, and bremsstrahlung, driven by a laser plasma accelerator. The analysis results in the measurement of x-ray energy spectra ranging from 10 keV to 1 MeV with peak flux greater than  $10^{10}$  photons/keV/Sr. The combined analysis methods provide a robust tool to accurately measure broadband x-ray sources (keV to MeV) driven by laser plasma acceleration with picosecond, kilojoule-class lasers.

Published under license by AIP Publishing. <https://doi.org/10.1063/1.5082965>

## I. INTRODUCTION

There is a need at large laser science facilities, e.g., the National Ignition Facility (NIF) and OMEGA, for compact, versatile x-ray sources to probe dense, transient states of matter created during high energy density (HED), inertial confinement fusion (ICF), and laboratory astrophysics studies. To date, research in x-ray source development at NIF and OMEGA has primarily focused on the development and improvement of laser-driven bremsstrahlung and K-alpha line emission backlighters.<sup>1–5</sup> The backlighter sources have been used to provide critical insight into various experimentally unexplored processes like shock propagation through materials,<sup>6</sup> instabilities in compressed gas,<sup>7</sup> and the shape and velocity of imploding

shells.<sup>8,9</sup> These sources commonly produce energies <20 keV with laser to x-ray conversion efficiencies of a less than a few percent in some materials and have large source sizes, >250  $\mu\text{m}$ .<sup>4,5,10</sup> The large source size from these backlighters can be mitigated with pinholes to reduce the effective source size and increase the resolution of radiographic images by sacrificing photon flux and contrast of the image.<sup>1,2</sup> An improved x-ray source to be used in similar experiments at NIF and OMEGA would need to have a broad energy range (few keV to MeV), high photon flux (> $10^{10}$  photons/keV/sr), and small source size (<20  $\mu\text{m}$ ).

X-rays with these improved characteristics can be produced from relativistic electrons generated in a self-modulated laser wakefield accelerator (SM-LWFA). A laser wakefield accelerator is

generated when an intense laser pulse interacts with a plasma, radially blowing out electrons through the ponderomotive force and generating a co-moving plasma wave. A powerful accelerating force is created through charge space separation in the plasma bubbles (100 GeV/m is typical) allowing trapped electrons to be accelerated to relativistic energies in a very short length. The SM-LWFA is a regime in which the laser pulse length is much greater than the plasma period, resulting in the pulse overlapping with multiple plasma periods.<sup>11</sup>

A SM-LWFA offers a compact means of generating relativistic electron beams<sup>11,12</sup> using existing picosecond lasers in operation at NIF (ARC), OMEGA (OMEGA-EP), LMJ (PETAL), and GEKKO (LFEX). The electrons produced in a SM-LWFA can be used to generate x-rays through several processes like betatron emission,<sup>13,14</sup> electron-driven bremsstrahlung radiation,<sup>15</sup> and inverse Compton scattering.<sup>16,17</sup>

Betatron x-rays are generated during the acceleration process in a SM-LWFA. Electrons trapped off axis and accelerated longitudinally also oscillate in the transverse direction due to space charge separation and produce x-rays in the laser propagation direction. Betatron x-rays from SM-LWFA and direct laser acceleration have been shown to reach photon fluxes  $>10^{10}$  photons/keV/sr with x-ray energies  $>15$  keV and a source size  $<35$   $\mu\text{m}$ .<sup>18,19</sup>

Inverse Compton scattering is produced when an electron collides with a photon up-shifted by  $2\gamma$  in the electron frame, where  $\gamma$  is the Lorentz factor of the electron. The electron oscillating in this Doppler shifted radiation field re-emits a photon, which in the laboratory frame is in the forward direction and is frequency up-shifted by an additional  $2\gamma$  for a total of  $4\gamma^2$ , in the case of head on collision. A common method of producing Compton x-rays in a laser wakefield experiment is to place a plasma mirror at the exit of the gas jet and reflect the drive laser pulse back onto the electrons.<sup>16</sup> In the SM-LWFA regime, this method can produce x-rays of energies  $>100$  keV with small source sizes  $<100$   $\mu\text{m}$  and high photon flux  $>10^8$  photons/keV/sr.<sup>20</sup>

Bremsstrahlung radiation is achieved by colliding the electron beam produced in a SM-LWFA with a high Z foil target. The electrons collide with the nuclei of the high Z foil producing high energy x-rays with a large divergence. Bremsstrahlung radiation produced through electron interactions has shown an increased x-ray generation efficiency over the previously discussed laser-generated bremsstrahlung sources and is capable of reaching temperatures of  $>1$  MeV with a photon flux  $>10^9$  photons/keV/sr.<sup>15,21</sup>

The optimization of x-ray emission properties, which vary based upon generation mechanism, motivates the development of robust analysis methods to be used for any SM-LWFA x-ray source in a spectral range between 10 keV and 1 MeV. This paper describes

three of them: forward fit, Ross pair, and differential average transmission (DAT), for three different diagnostics, each sensitive to a different range of x-ray energies (thin filters, stacked image plate spectrometer,<sup>22</sup> and step wedge<sup>23</sup>). This paper is organized as follows: Sec. II presents an overview of the experiments; Sec. III details and compares each of the analysis methods and diagnostics using a laser-driven bremsstrahlung source; Sec. IV applies these methods and diagnostics to quantify x-ray sources driven by SM-LWFA on a  $>100$  J, ps laser system, the Titan Laser at Lawrence Livermore National Laboratory (LLNL).

## II. EXPERIMENTAL OVERVIEW

The Titan laser, located at the Jupiter Laser Facility (JLF) at the Lawrence Livermore National Laboratory (LLNL), has a beam energy of 120 J, a pulse length of  $0.7_{-0.1}^{+0.3}$  ps, and a central wavelength of 1053 nm. In our experiment, shown in Fig. 1, the laser is focused 1 mm above a 4 mm He gas jet using a  $F/10$  off axis parabolic mirror to obtain a spot size of  $\sim 29$   $\mu\text{m}$  and an intensity of  $\sim 10^{19}$  W/cm<sup>2</sup>. The laser pulse ionizes the He gas and creates a plasma with a density of  $\sim 5 \times 10^{18}$  cm<sup>-3</sup> and drives a SM-LWFA, which produces a beam of electrons with a maximum energy of  $\sim 380$  MeV. Betatron x-rays are generated during the acceleration of electrons in the SM-LWFA, and by placing a 100  $\mu\text{m}$  polyethylene target at the exit of the jet or a 500  $\mu\text{m}$  W target 15 mm from the exit of the gas jet, inverse Compton scattered or bremsstrahlung x-rays are generated, respectively. The electrons produced in the SM-LWFA are bent away from the propagation axis using a 0.9 T magnetic spectrometer. The electron signal is captured on a Fujifilm BAS-IP MS image plate (IP), the type of IP used for all the diagnostics, and an energy spectrum is determined by mapping the displacement in the horizontal direction on the IP to the expected location given the spectrometer calibration.

The x-rays exit the target chamber via a 200  $\mu\text{m}$  mylar window located 1.5 m from the gas jet and enter the filter wheel, Fig. 2(a), located 4 cm from the mylar window. The filter wheel is a set of 10 materials, differing in thicknesses, that are sensitive to x-ray energies up to  $\sim 40$  keV. The transmission of all the channels, shown in Fig. 3, reaches 100% at roughly 40 keV, preventing x-rays above this energy to be differentiated. The materials, thicknesses, and channel number are detailed in Fig. 2(a). The transmitted x-ray signal is collected by an IP placed at the back of the filter wheel. The x-rays pass through the filter wheel and into the cannon, shown in Fig. 2(b), which uses 8 filters stacked behind one another with an IP between each material to capture the x-ray signal in each layer.<sup>22,24</sup> The cannon is sensitive to a higher energy range, 30 to  $\sim 200$  keV, and is used in tandem with the filter wheel to improve the energy detection range. For higher

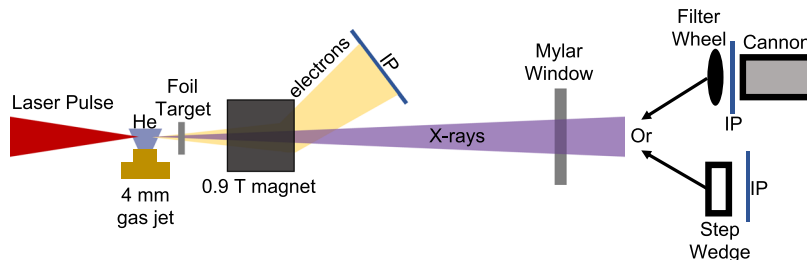


FIG. 1. Experimental setup for SM-LWFA experiment on the Titan Laser at JLF.

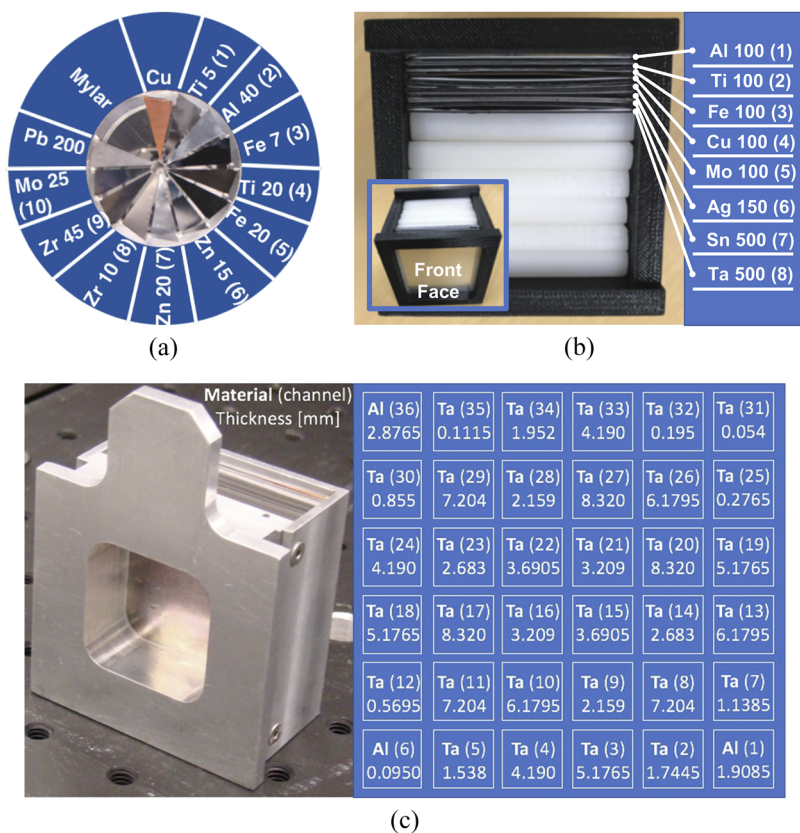


FIG. 2. (a) The filter wheel diagnostic channels are labeled clockwise from the top right, each corresponding to a different material and thickness. The image is labeled with the material type, thickness in  $\mu\text{m}$ , and the channel number, respectively. (b) The cannon diagnostic channels are labeled from the front of the detector to the back, each corresponding to a different material and thickness, labeled with the material type, thickness in  $\mu\text{m}$ , and channel number, respectively. The inset shows a view of the cannon from the front. (c) The step wedge diagnostic uses varying thicknesses of Ta to attenuate the x-ray signal.

expected x-ray energies (up to a few MeV), the step wedge diagnostic replaces both the filter wheel and cannon along the beam axis. The step wedge uses stacked plates of Ta with holes cut into them creating channels of varying thickness to alter the x-ray attenuation through each. The signal is then collected on an IP placed behind the diagnostic.<sup>23</sup>

The IPs are all scanned using a Fuji model FLA7000 scanner at a  $200 \mu\text{m}$  pixel size. The scanner provides a measure of counts per pixel that is then converted to photo stimulated luminescence (PSL) using the calibration equation provided by Ref. 25.

### III. ANALYSIS METHODS

This section presents the diagnostics results and associated analysis methods in the case of a laser-driven bremsstrahlung source. Laser-driven bremsstrahlung is used here because it is a well understood x-ray production mechanism that can be generated without creating additional x-ray noise. To ensure only laser bremsstrahlung is generated, the gas jet is not operated for these shots ensuring there is no LWFA generation. The laser focus is positioned 1 mm into the entrance of the 4 mm gas jet and a  $100 \mu\text{m}$  Al target was placed at the exit of the jet, 3 mm from laser focus, so that the focal spot size is  $\sim 50 \mu\text{m}$  and the laser intensity is  $2 \times 10^{18} \text{ W/cm}^2$ .

#### A. Forward fit method

The forward fit method uses the x-ray attenuation properties of thin filters to fit a measured set of data and extrapolate the energy spectrum using an assumed analytical distribution function.<sup>18,19,21</sup> Equation (1) describes how to calculate a synthetic PSL value for each material using an assumed analytical distribution function,  $f_{E,A}(E_\gamma)$ , and a material response function,  $Y_i(E_\gamma)$ , shown in Fig. 3

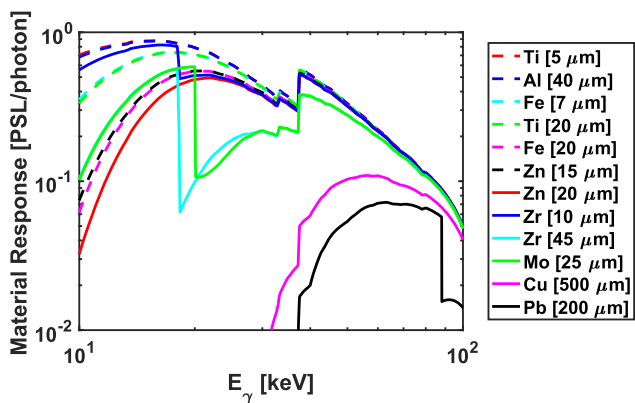
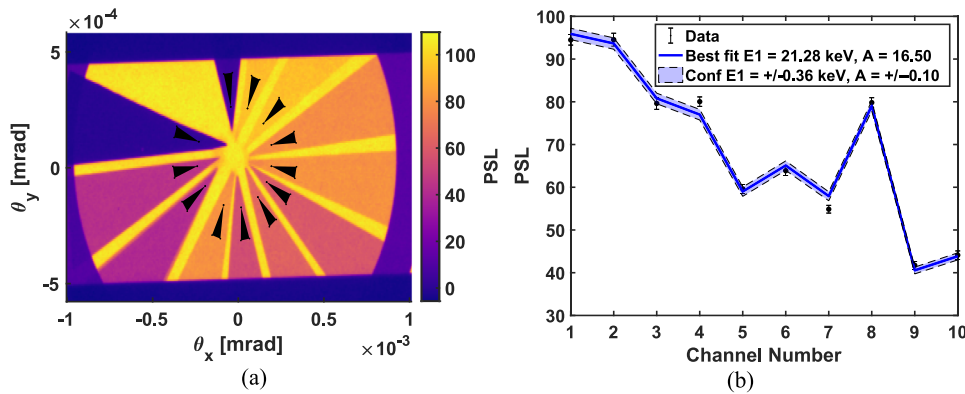


FIG. 3. Filter wheel material response curves as a function of x-ray energy converted to PSL/photon.



**FIG. 4.** (a) Raw data of the filter wheel diagnostic on bremsstrahlung x-ray data. The black triangles show the areas in which the data was sampled to obtain mean PSL values for the fit. (b) Results of the forward fit method on bremsstrahlung x-ray data described in the text.

$$Y_i(E_\gamma) = T_i \times IP_{resp}, \quad (1)$$

$$PSL_i = \int Y_i f_{E,A} dE_\gamma \times \theta,$$

where  $T_i$  is the calculated transmission of material  $i$ ,  $IP_{resp}$  is the response function of the image plate,<sup>26</sup>  $E_\gamma$  is the photon energy, and  $\theta$  is the angle subtended by each pixel from the source. The material response is a product of each material the x-rays interact with on the way to the detector and the energy-dependent response of the detector used. Here,  $f_{E,A}$  is the chosen analytical distribution function to describe the x-ray generation mechanism where  $E$  is the energy and  $A$  the amplitude. Calculated PSL values are fit to a measured data set by varying the amplitude and energy using weighted least squares fitting tools.

Bremsstrahlung emission is modeled with a single temperature distribution function,  $f_{E,A} = A \times 10^{10} \times e^{-E_\gamma/E}$ , that is used with Eq. (1) to calculate a PSL value for each channel. An example, a laser-driven bremsstrahlung source measured with the thin filter wheel, is shown in Fig. 4. The best fit for this laser bremsstrahlung data results in a temperature of  $21.2 \pm 0.36$  keV with an amplitude of  $16.5 \pm 0.10$ , giving a total flux of  $16.5 \pm 0.10 \times 10^{10}$  photons/keV/sr, plotted in blue in Fig. 4(b). The mean PSL signal for each material is taken from within the area of each small triangle shown in Fig. 4(a) and plotted as black data points in Fig. 4(b). The error in PSL is the standard deviation of the signal in each channel. The error in temperature,  $E1$ , and amplitude,  $A$ , are obtained from the best fit of the upper and lower error in PSL.

## B. Ross pair method

The materials that make up the filter wheel were designed to take advantage of the Ross pair analysis method.<sup>27</sup> Each material was chosen such that the K-edge location and thickness would provide a difference in signal equal to zero everywhere except for a small energy bin determined by the difference in K-edge location. The thickness of each material controls the total attenuation of the x-ray signal and can be used to ensure that the signal outside each bin is as close to zero as possible. By choosing materials correctly, the Ross pair method can provide a direct measurement of x-ray flux in a small energy range. Figure 5 shows the energy bins for the materials in the filter wheel diagnostic used in our experiment and the attenuation of the signal in each bin. By subtracting channels 1-2,

3-4, 6-5, 8-7, and 10-9 corresponding to  $5 \mu\text{m}$  Ti- $40 \mu\text{m}$  Al,  $7 \mu\text{m}$  Fe- $20 \mu\text{m}$  Ti,  $15 \mu\text{m}$  Zn- $20 \mu\text{m}$  Fe,  $10 \mu\text{m}$  Zr- $20 \mu\text{m}$  Zn, and  $25 \mu\text{m}$  Mo- $45 \mu\text{m}$  Zr, the flux in 5 energy bins spanning 3–20 keV can be directly measured.

As can be seen on the blue curve in Fig. 5, the signal outside the bin is not always exactly zero, which accounts for error in the photon number measurement. The ratio of integrated signal outside/inside is calculated as the error in photon count.

The difference in PSL values from the filter wheel data in Fig. 4(a), following the same subtraction scheme that created Fig. 5, is converted to photon flux by following Eq. (2)

$$\left[ \frac{d^2 N}{dE d\Omega} \right]_i = \frac{PSL_i}{T_{r_i}^{mean} \times IP_i^{mean} \times \theta \times W_i^{bin}}. \quad (2)$$

Here  $T_{r_i}^{mean}$  is the mean transmission value of each bin,  $IP_i^{mean}$  is the mean image plate response value for each bin,  $\theta$  is the angle subtended by each pixel from the source, and  $W_i^{bin}$  is the bin width in keV.

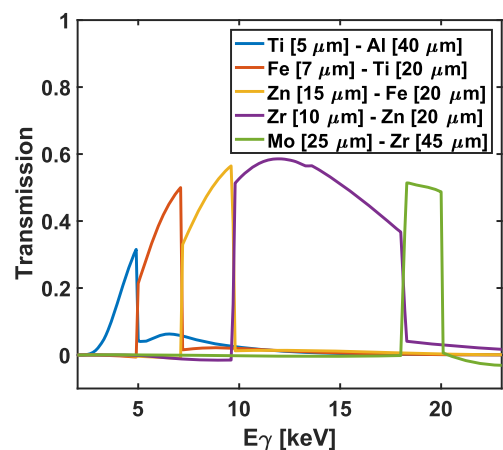


**FIG. 5.** Subtraction of channels 1-2, 3-4, 6-5, 8-7, and 10-9 corresponding to  $5 \mu\text{m}$  Ti- $40 \mu\text{m}$  Al,  $7 \mu\text{m}$  Fe- $20 \mu\text{m}$  Ti,  $15 \mu\text{m}$  Zn- $20 \mu\text{m}$  Fe,  $10 \mu\text{m}$  Zr- $20 \mu\text{m}$  Zn, and  $25 \mu\text{m}$  Mo- $45 \mu\text{m}$  Zr results in the remaining signal appearing in small energy bins.

### C. Differential averaged transmission method (DAT)

The DAT method<sup>16</sup> is similar to the Ross pair method in that it utilizes the subtraction of the transmission signal from two different materials to provide a measured data point and does not rely on a particular spectral distribution. This method works well when materials in the diagnostic are the same element with varying thicknesses but may provide poor results when subtracting different elements due to the different K-edge locations. The subtracted material transmission curves of the desired materials should create a broad distribution for this method to work properly.

Figure 6 shows this method applied to the filter wheel diagnostic. The energy assigned to each pair corresponds to the mean energy of that pair's distribution. The bin size, corresponding to the region which contains 50% of the pair's signal, is plotted as the error in energy. The error in photon flux is determined by integrating the signal outside of the energy bin and converting the results to percentages of the total signal. The percentages are used to represent the error in measured photon flux caused by excluding the regions outside of the 50% energy bin in the calculation.

The photon number is then calculated as follows:

$$\left[ \frac{d^2N}{dEd\Omega} \right]_k = \frac{(S_1 - S_2)}{\int f_k dE_\gamma}, \quad (3)$$

$$f_k = (T_1 - T_2) \times R \times \theta.$$

Here, N is the number of photons, dE is per photon energy, dΩ is per solid angle, S<sub>1,2</sub> are the measured signals being subtracted, T<sub>1,2</sub> are the calculated transmission curves through the same materials, R is the response of the detector being used, and θ is the angle subtended by each pixel in the detector.

By using the PSL values shown in Fig. 4 and the filter wheel material pairs described in Fig. 6, the photon flux is calculated and plotted in Fig. 7 along with the results of the Ross pair method. As shown in Fig. 5, there are five possible data points which can be calculated using the Ross pair method; however, Fig. 7 only

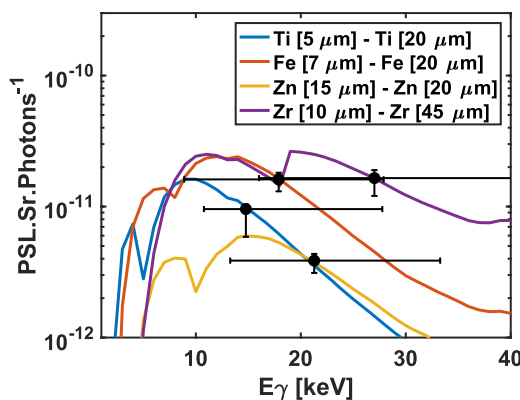


**FIG. 6.** DAT bins are created by subtracting channels 1-4, 3-5, 6-7, and 9-10 corresponding to 5 μm Ti-20 μm Ti, 7 μm Fe-20 μm Fe, 15 μm Zn-20 μm Zn, and 10 μm Zr-45 μm Zr resulting in broad transmission distributions. The mean energy and full width half maximum are determined for each distribution and are used for error calculation. See the text for details.

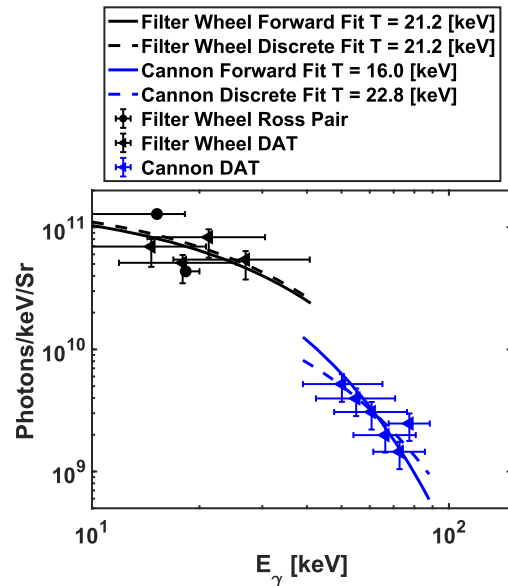


**FIG. 7.** Results of forward fitting (solid) and discrete fitting (dashed) analysis for a laser-driven bremsstrahlung source using the filter wheel (black), and cannon (blue) diagnostics. Data points are the result of Ross pair (circles) and DAT (triangles) analysis methods described in the text.

has two data points plotted. The missing data points are from the first three low energy pairs which, when created through subtracting the signal from the pair's corresponding materials, resulted in a zero or negative flux. This can be caused either by x-rays with energies above the pair's sensitivity region, or by low energy x-rays which are blocked on the way to the detector. In this experiment, we were unable to resolve the Ross pair signals below 10 keV due to the mylar window on the target chamber attenuating the signal of low energy x-rays to a level below our detection threshold.

### D. Fitting the discrete data points

The discrete data points, determined by the Ross pair and DAT methods, are fit using weighted least squares fitting tools and the same distribution function as the forward fit method, and  $f_{E1,A} = A \times 10^{10} \times e^{-E_\gamma/E1}$  for a laser-driven bremsstrahlung source. This fit provides an additional independent method of determining the temperature and amplitude of the x-ray energy spectrum. The best fit results in a temperature and amplitude of  $E1 = 21.2 \pm 4.23$  ( $22.9 \pm 0.67$ ) keV  $A = 15.9 \pm 0.62$  ( $4.5 \pm 1.15$ ) photons/keV/sr for the filter wheel (cannon) diagnostic, shown in black in Fig. 7. The error in the temperature, E1, and amplitude, A, of this fit is determined through the best fit of the upper and lower photon flux errors of the discrete data set. The energy bins, represented by energy error bars, are not explicitly included in the fitting as the flux error accounts for signal not included within this bin. If the energy bin gets bigger or smaller, the flux error will change by an equal percentage to compensate, as detailed in Sec. III C. Like the discrete data points, their fits agree very well with the forward fit results inside each detectors sensitivity range.

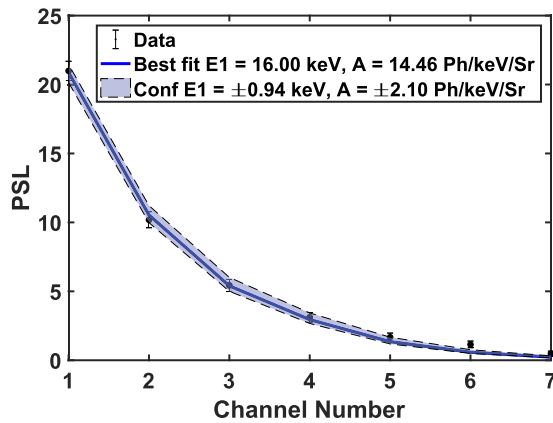


FIG. 8. Results of the forward fitting method using the cannon diagnostic. Here  $E_1$  is the temperature and  $A$  is the amplitude of the single temperature distribution.

### E. Stacked image plate spectrometer analysis

Subsections III A–III D have detailed three analysis methods applied to a bremsstrahlung source using the filter wheel diagnostic. This section will apply the same analysis methods to the cannon, a stacked image plate spectrometer, and highlight the differences between the two diagnostics. As shown in Fig. 1, the cannon can be fielded at the same time as the filter wheel allowing for a greater range of the x-ray spectrum to be measured. Similar to Sec. III A, Fig. 8 shows the results of the forward fitting method, where the channels are detailed in Fig. 2(b). The bremsstrahlung energy spectrum was again modeled using a single temperature distribution,  $f(E_1, A) = A \times 10^{10} \times e^{-E_\gamma/E_1}$ , and resulted in a temperature  $E_1 = 16.0 \pm 2.17$  keV and amplitude  $A = 13.44 \pm 3.9$  Photons/keV/Sr as shown in Fig. 7. The DAT method is computed the same way as in Subsection III C; however, since the cannon has stacked materials,  $S_i$  and  $T_i$  as defined in Eq. (3) represent channels rather than materials. For example, channel 1 is Al and channel 2 is  $100 \mu\text{m}$  Al  $\times$  image plate transmission  $\times 100 \mu\text{m}$  Ti. The resulting measured x-ray energies are shown in blue in Fig. 7 with the forward fit results.

### F. Combining methods and diagnostics

Sections III A–III E have detailed three separate methods of analyzing measured x-ray energy spectra and shown the methods applied to two diagnostics. Applying the three methods to measured x-ray data results in two valid temperature and amplitude solutions. Optimally, the two solutions will exactly agree with one another. However, due to noise in the raw data, the solutions more often will be different. Therefore, the results are combined to produce a solution band which encompasses the results from both fitting methods, forward fit and discrete fit. The results of both fits are plotted with their maximum and minimum errors, and the highest and lowest solution, regardless of the fitting method, is chosen. The two temperature and amplitude solutions are then presented as the final measured x-ray energy spectrum.

As an example, Fig. 9 shows the solution band for the filter wheel (black) and the cannon (blue) on the same laser-driven bremsstrahlung shot. The solution band for the filter wheel is created

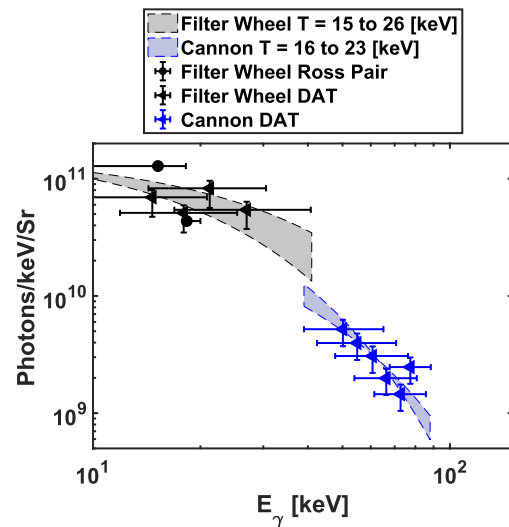


FIG. 9. The solution bands for a laser bremsstrahlung source. The bands are created by combining forward fitting and discrete fitting as explained in the text.

by combining the lowest ( $T = 15.0$  keV and  $A = 16.01$  photons/keV/sr) and the highest ( $T = 26$  keV and  $A = 15.28$  photons/keV/sr) temperature and amplitude fit from the forward fit and discrete fit methods. In this instance, the discrete fit fully encompasses the forward fit solution and error, so both the highest and lowest temperature and amplitude solutions are from the discrete fit.

The same method of choosing the highest and lowest fit is then applied to the cannon diagnostic resulting in temperatures,  $T$ , of 16 and 23 keV and amplitudes,  $A$ , of 16.6 and 3.8 photons/keV/sr from the forward fit and discrete fit, respectively. The cannon solution band is then combined with the filter wheel solution band to create a measured x-ray spectrum spanning 10–100 keV.

## IV. SM-LWFA X-RAY SOURCES

This section presents the analysis of x-ray sources generated through SM-LWFA following the experimental schemes shown in Fig. 10. X-ray characterization from SM-LWFA generated sources that generally have far more noise to mitigate than the laser-only bremsstrahlung data presented above due to the large amount of charge being diverted into the target chamber walls, and proper accounting for this noise is instrumental in correctly determining the energy spectrum of LWFA-driven x-ray sources. The filter wheel diagnostic includes a  $500 \mu\text{m}$  Cu and  $200 \mu\text{m}$  Pb filter to be used for background subtraction. These filters prevent any transmitted signal from x-rays above  $\sim 40$  keV from contributing to the overall data. Since the sensitivity of the filter wheel has a maximum of  $\sim 40$  keV, any signal behind these filters can be assumed as background. For data with a uniform background level, the signal level from behind the Cu and Pb filters is subtracted from the whole image to reduce the noise level and improve accuracy of the analysis. For non-uniform backgrounds, a mask is created by selecting the perimeter of each filter and removing it from the image as shown in Fig. 11. The background is smoothed over the whole image and normalized

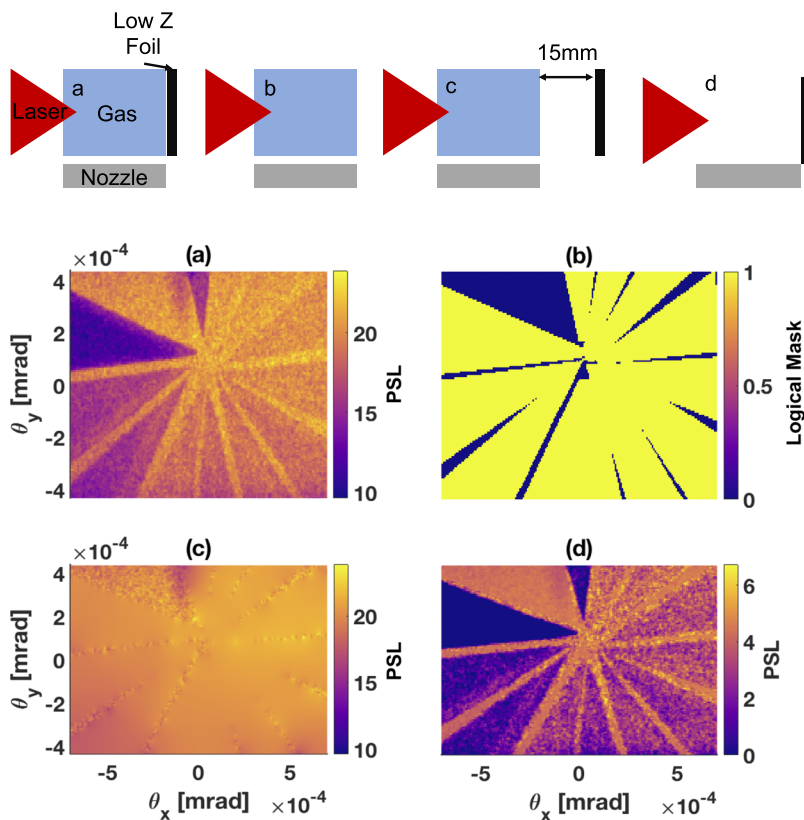


**FIG. 10.** Experimental setup for each SM-LWFA x-ray generation mechanism: (a) inverse Compton, (b) betatron, (c) electron-driven bremsstrahlung, and (d) laser-driven bremsstrahlung. Each method is isolated by controlling the gas and foil placement as detailed in the text.

**FIG. 11.** (a) Experimental data with no background subtraction. (b) 2D mask created to remove filters from the background signal. (c) Using the 2D mask, the background signal is smoothed over the filter regions and normalized to the PSL signal behind the copper or lead filter. (d) The final image after subtracting the smoothed background from the original image.

such that the maximum value of the smoothed image is equal to the signal behind the Cu or Pb filter. The smoothed image is subtracted from the main image to remove non-uniform backgrounds, vastly improving the accuracy of the analysis methods detailed above.

### A. Betatron radiation

Here, betatron radiation is generated during the SM-LWFA electron acceleration process. The laser is focused as described in Sec. II with no foil placed after the gas jet [Fig. 10(b)]. The data analysis begins by first following the background subtraction technique detailed in Fig. 11 and then applying the three analysis methods described in Sec. III. Figure 12 shows the results of these methods using  $f_{E1,A} = A \times 10^{10} \frac{E_y}{E1^2} K_{\frac{2}{3}}^2 \left[ \frac{E_y}{E1} \right]$ <sup>13,28</sup> as the analytic equation describing the x-ray energy spectrum. The expected energy range for betatron radiation is  $<40$  keV due to the critical energy scaling ( $\sim 5 \times 10^{-21} \gamma^2 n_e [\text{cm}^{-3}] r_0 [\mu\text{m}]$ ) where the maximum electron energy is measured to be  $\sim 300$  MeV, so the filter wheel and cannon diagnostics were used. The noise in this signal is higher than the laser bremsstrahlung example due to the large non-uniform background produced from stray electrons in the target chamber. The combined analysis methods result in a critical energy (the point in which half the energy in the spectrum lies below this value), E1, between 25 and 34 keV and an amplitude, A, between 15.7 and 16.5 photons/keV/sr. This result is combined with the Ross pair (circles) and DAT (triangles) methods in Fig. 12. Due to noise in the later channels of the

cannon diagnostic which could not be mitigated, the cannon did not provide fitted critical energies to combine with the filter wheel results.

### B. Inverse Compton scattering

We generate inverse Compton radiation by placing a  $100 \mu\text{m}$  polyethylene target at the exit of the gas jet as shown in Fig. 10(a). The laser, after generating the SM-LWFA and accelerating electrons, exits the gas jet and ionizes the polyethylene target, creating a plasma mirror.<sup>16</sup> The laser pulse is reflected back onto the relativistic electrons, producing x-rays in the electron propagation direction. Here, we have contribution from four different mechanisms: betatron from the SM-LWFA, bremsstrahlung from interaction of the laser and the electrons with the foil, and the Compton radiation we seek to measure. To account for the x-rays generated from the first three mechanisms, we measure the radiation energy spectrum produced by isolated betatron,  $f_{\text{Beta}}$ , and bremsstrahlung,  $f_{\text{Brem}}$ , emissions under the same experimental conditions and include the results in the Compton analysis. The laser-driven and electron-driven bremsstrahlung components are differentiated by placing the foil at the exit and 15 mm from the exit of the gas jet, respectively, as shown in Fig. 10. In the latter case, the laser has diverged more than the electron beam ensuring the electron-driven bremsstrahlung is dominant.

Compton scattering is likely to produce higher energy x-rays than betatron radiation, as inverse Compton scattering scales as

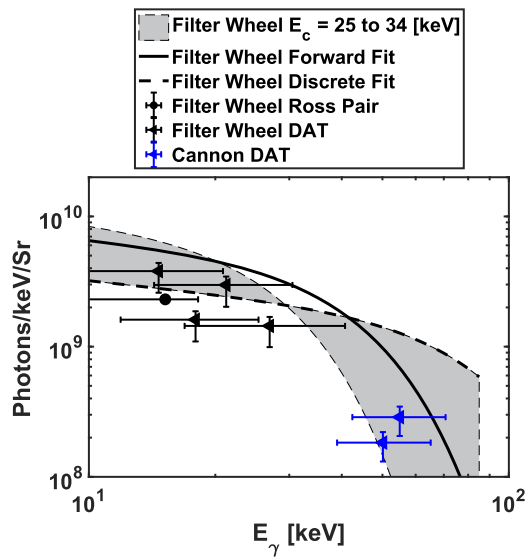


**FIG. 12.** Combining the forward fit, Ross pair, and DAT analysis methods from the filter wheel and cannon diagnostics creates a band of solutions between critical energies of 25 and 34 keV using the filter wheel diagnostic. Only the first three channels of the cannon had signal above the detection threshold, resulting in two data points using the DAT method. These data points are not sufficient to use the fitting method but are plotted here to show agreement with the filter wheel solution band, which is extrapolated to 65 keV.

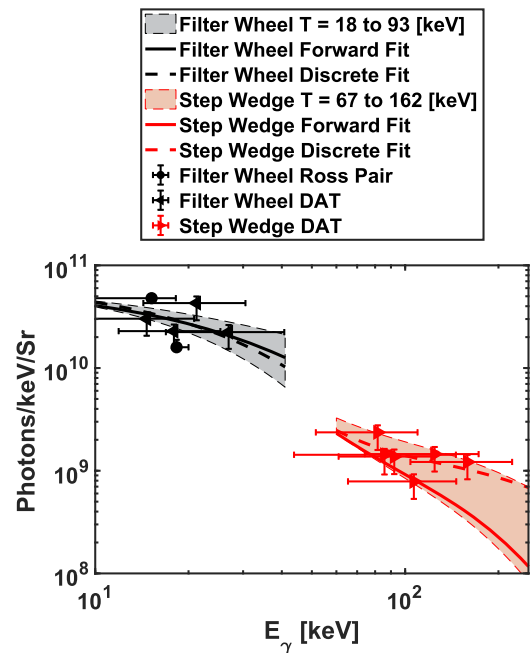


**FIG. 13.** The filter wheel (black) and step wedge (red) were used to measure the low and high energy regions of the inverse Compton x-ray spectrum respectively. The filter wheel measured a temperature band of 18–93 keV in the 10–40 keV region, while the step wedge measured a temperature band of 67–162 keV between 60 and 250 keV.

$\sim 4\gamma^2 E_l$ , where  $E_l$  is the laser photon energy, and betatron radiation drops exponentially after its critical energy  $5 \times 10^{-21} \gamma^2 n_e [\text{cm}^{-3}] r_0 [\mu\text{m}]$ . Hence, we use the step wedge.<sup>14</sup> A single temperature spectrum,  $f_{E1,A} = f_{\text{Beta}} + f_{\text{Brem}} + A \times 10^{10} e^{-\frac{E_\gamma}{T}}$ , is used for the forward fit and discrete fit methods after first using the background subtraction technique detailed in Fig. 11. The Compton emission is approximated as a single temperature distribution in the narrow range of sensitivity for both the filter wheel and step wedge. The resulting temperature bands, found by following the analysis methods described in Sec. III, are shown in Fig. 13 to be  $E1 = 18\text{--}93$  keV and  $E1 = 67\text{--}162$  keV between 10–40 keV and 60–250 keV, respectively. These sensitivity regions are dictated by the diagnostics and not the spectrum being measured. The lower energy region measured by the filter wheel has large components of laser bremsstrahlung and betatron signal, however, the signal in the higher energy region measured by the step wedge can only be x-rays produced through inverse Compton.<sup>20</sup>

### C. Electron bremsstrahlung radiation

Electron-driven bremsstrahlung radiation is generated by colliding the relativistic electrons from a SM-LWFA with a 500  $\mu\text{m}$  thick W target placed 15 mm from the exit of the gas jet, mitigating laser bremsstrahlung and inverse Compton emissions, as shown in Fig. 10(c). A 500  $\mu\text{m}$  target is chosen for this mechanism to convert as much of the electron energy into x-rays as possible, without being too thick so that x-rays are re-absorbed. By choosing the correct high-Z foil, much of the electron energy can be converted to x-rays through collisions in the foil, producing a high temperature (MeV)

emission spectrum. Due to the expected high energy x-ray production, the step wedge diagnostic is used to analyze the electron-driven bremsstrahlung emission spectrum. The temperature bands for this mechanism are found to be  $T = 806\text{--}1354$  keV by fitting to a single temperature distribution,  $f_{E1,A} = A \times 10^{10} e^{-\frac{E_\gamma}{T}}$ , following the analysis methods detailed in Sec. III. The result of this analysis is plotted with data points following the DAT method in Fig. 14.

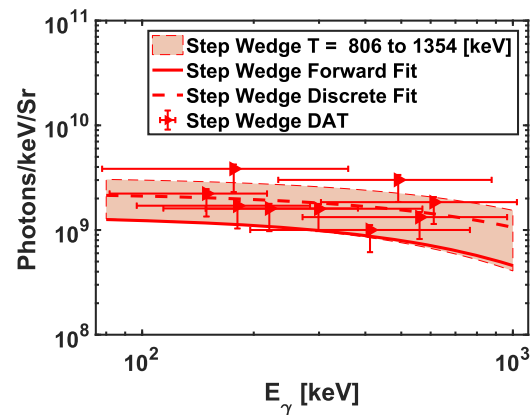


**FIG. 14.** The forward fit and discrete fit for electron-driven bremsstrahlung x-rays produce a solution band with temperatures between 806 and 1354 keV (red shaded region).

## V. CONCLUSION

In conclusion, we have shown the analysis methods employed to fully characterize x-ray energy spectra generated through SM-LWFA. These methods were applied to three diagnostics, each sensitive to a different energy range: the filter wheel (10–40 keV), cannon (30–80 keV), and step wedge (60 keV to >1 MeV). These diagnostics were used together to characterize four distinct x-ray generation mechanisms: betatron, laser and electron driven bremsstrahlung, and inverse Compton scattering. These x-ray sources span a total energy range of more than 1 MeV, proving useful in a wide variety of applications.

The forward fit method provides a way to extrapolate an energy spectrum given an analytical function to describe the x-ray energy distribution. The Ross pair and DAT methods provide a way to directly measure the photon flux in a narrow energy bin without needing to assume a distribution function. These discrete points are then fit using the same equation used in forward fitting to provide a separate independent measure of the x-ray energy spectrum. Combining all of these methods provides a solution band in which the x-ray spectrum can exist. This technique allows a robust method of characterizing an x-ray source in a high noise environment, like that of SM-LWFA.

Large laser facilities like NIF and OMEGA are capable of creating experimentally unexplored conditions and states of matter valuable to HED, ICF, and laboratory astrophysics. These new experimental capabilities bring with them a need for a broadband x-ray source capable of probing the various transient states of matter being created. Laser wakefield accelerators are a promising tunable driver for x-ray sources at these facilities and have been demonstrated to produce a broad range of x-ray energies.

## ACKNOWLEDGMENTS

This work was performed under the auspices of the U.S. Department of Energy by the Lawrence Livermore National Laboratory under Contract No. DE-AC52-07NA27344, supported by the LLNL LDRD program under tracking code 16-ERD-024, the DOE Office Science Early Career Research Program (Fusion Energy Sciences) under SCW 1575-1, the Air Force Office of Scientific Research No. FA9550-14-1-0045, the U.S. Department of Energy/National Science Foundation under Award No. DE-SC0017950, NNSA Grant No. DE-NA0002950, and the DOE Grant No. DE-SC0010064. We acknowledge the support of the Jupiter Laser Facility staff at LLNL for operating the Titan laser.

## REFERENCES

- <sup>1</sup>C. M. Huntington, C. M. Krauland, C. C. Kuranz, R. P. Drake, H.-S. Park, D. H. Kalantar, B. R. Maddox, B. A. Remington, and J. Kline, *Rev. Sci. Instrum.* **81**, 10E536 (2010).
- <sup>2</sup>C. C. Kuranz, B. E. Blue, R. P. Drake, H. F. Robey, J. F. Hansen, J. P. Knauer, M. J. Grosskopf, C. Krauland, and D. C. Marion, *Rev. Sci. Instrum.* **77**, 10E327 (2006).
- <sup>3</sup>R. Hollinger, C. Bargsten, V. N. Shlyaptsev, V. Kaymak, A. Pukhov, M. G. Capeluto, S. Wang, A. Rockwood, Y. Wang, A. Townsend, A. Prieto, P. Stockton, A. Curtis, and J. J. Rocca, *Optica* **4**, 1344 (2017).
- <sup>4</sup>M. Barrios, K. Fournier, S. Regan, O. Landen, M. May, Y. Opachich, K. Widmann, D. Bradley, and G. Collins, *High Energy Density Phys.* **9**, 626 (2013).

- <sup>5</sup>D. Babonneau, M. Primout, F. Girard, J.-P. Jadaud, M. Naudy, B. Villette, S. Depierreux, C. Blancard, G. Faussurier, K. B. Fournier, L. Suter, R. Kauffman, S. Glenzer, M. C. Miller, J. Grn, and J. Davis, *Phys. Plasmas* **15**, 092702 (2008).
- <sup>6</sup>A. B. Reighard, R. P. Drake, K. K. Dannenberg, D. J. Kremer, M. Grosskopf, E. C. Harding, D. R. Leibbrandt, S. G. Glendinning, T. S. Perry, B. A. Remington, J. Greenough, J. Knauer, T. Boehly, S. Bouquet, L. Boireau, M. Koenig, and T. Vinci, *Phys. Plasmas* **13**, 082901 (2006).
- <sup>7</sup>B. E. Blue, H. F. Robey, S. G. Glendinning, M. J. Bono, S. C. Burkhart, J. R. Celeste, R. F. Coker, R. L. Costa, S. N. Dixit, J. M. Foster, J. F. Hansen, C. A. Haynam, M. R. Hermann, J. P. Holder, W. W. Hsing, D. H. Kalantar, N. E. Lanier, D. A. Latray, H. Louis, B. J. MacGowan, G. R. Maggelssen, C. D. Marshall, E. I. Moses, A. J. Nikitin, D. W. O'Brien, T. S. Perry, M. W. Poole, V. V. Rekow, P. A. Rosen, M. B. Schneider, P. E. Stry, B. M. V. Wonterghem, R. Wallace, S. V. Weber, B. H. Wilde, D. T. Woods, and B. K. Young, *Phys. Plasmas* **12**, 056313 (2005).
- <sup>8</sup>F. J. Marshall, P. W. McKenty, J. A. Delettrez, R. Epstein, J. P. Knauer, V. A. Smalyuk, J. A. Freije, C. K. Li, R. D. Petrasso, F. H. Séguin, and R. C. Mancini, *Phys. Rev. Lett.* **102**, 185004 (2009).
- <sup>9</sup>J. R. Rygg, O. S. Jones, J. E. Field, M. A. Barrios, L. R. Benedetti, G. W. Collins, D. C. Eder, M. J. Edwards, J. L. Kline, J. J. Kroll, O. L. Landen, T. Ma, A. Pak, J. L. Peterson, K. Raman, R. P. J. Town, and D. K. Bradley, *Phys. Rev. Lett.* **112**, 195001 (2014).
- <sup>10</sup>C. Courtois, R. Edwards, A. Compant La Fontaine, C. Aedy, S. Bazzoli, J. L. Bourgade, J. Gazave, J. M. Lagrange, O. Landoas, L. L. Dain, D. Mastro Simone, N. Pichoff, G. Pien, and C. Stoeckl, *Phys. Plasmas* **20**, 083114 (2013).
- <sup>11</sup>A. Modena, Z. Najmudin, A. E. Dangor, C. E. Clayton, K. A. Marsh, C. Joshi, V. Malka, C. B. Darrow, C. Danson, D. Neely, and F. Walsh, *Nature* **377**, 606 (1995).
- <sup>12</sup>E. Esarey, C. B. Schroeder, and W. P. Leemans, *Rev. Mod. Phys.* **81**, 1229 (2009).
- <sup>13</sup>E. Esarey, B. A. Shadwick, P. Catravas, and W. P. Leemans, *Phys. Rev. E* **65**, 056505 (2002).
- <sup>14</sup>A. Rousse, K. Phuoc, R. Shah, A. Pukhov, E. Lefebvre, V. Malka, S. Kiselev, F. Burgy, J. Rousseau, and D. Umstadter, *Phys. Rev. Lett.* **93**, 135005 (2004).
- <sup>15</sup>Y. Glinec, J. Faure, L. L. Dain, S. Darbon, T. Hosokai, J. J. Santos, E. Lefebvre, J. P. Rousseau, F. Burgy, B. Mercier, and V. Malka, *Phys. Rev. Lett.* **94**, 025003 (2005).
- <sup>16</sup>K. T. Phuoc and S. Corde, *Nat. Photonics* **6**, 308 (2012).
- <sup>17</sup>W. Yan, C. Fruhling, G. Golovin, D. Haden, J. Luo, P. Zhang, B. Zhao, J. Zhang, C. Liu, M. Chen, S. Chen, S. Banerjee, and D. Umstadter, *Nat. Photonics* **11**, 514 (2017).
- <sup>18</sup>F. Albert, N. Lemos, J. L. Shaw, B. B. Pollock, C. Goyon, W. Schumaker, A. M. Saunders, K. A. Marsh, A. Pak, J. E. Ralph, J. L. Martins, L. D. Amorim, R. W. Falcone, S. H. Glenzer, J. D. Moody, and C. Joshi, *Phys. Rev. Lett.* **118**, 134801 (2017).
- <sup>19</sup>S. Kneip, S. R. Nagel, C. Bellei, N. Bourgeois, A. E. Dangor, A. Gopal, R. Heathcote, S. P. D. Mangles, J. R. Marques, A. Maksimchuk, P. M. Nilson, K. T. Phuoc, S. Reed, M. Tzoufras, F. S. Tsung, L. Willingale, W. B. Mori, A. Rousse, K. Krushelnick, and Z. Najmudin, *Phys. Rev. Lett.* **100**, 105006 (2008).
- <sup>20</sup>N. Lemos, P. M. King, J. L. Shaw *et al.* "Ultra-broad-band, inverse Compton scattering source using a picosecond laser-driven plasma accelerator," *Phys. Rev. Lett.* (submitted).
- <sup>21</sup>N. Lemos, F. Albert, J. L. Shaw, D. Papp, R. Polanek, P. King, A. L. Milder, K. A. Marsh, A. Pak, B. B. Pollock, B. M. Hegelich, J. D. Moody, J. Park, R. Tommasini, G. J. Williams, H. Chen, and C. Joshi, *Plasma Phys. Controlled Fusion* **60**, 054008 (2018).
- <sup>22</sup>C. D. Chen, J. A. King, M. H. Key, K. U. Akli, and F. N. Beg, *Rev. Sci. Instrum.* **79**, 10E305 (2008).
- <sup>23</sup>G. J. Williams, R. Tommasini, N. Lemos, J. Park, and H. Chen, *Rev. Sci. Instrum.* **89**, 10F116 (2018).
- <sup>24</sup>F. Albert, A. G. R. Thomas, S. P. D. Mangles, S. Banerjee, S. Corde, A. Flacco, M. Litos, D. Neely, J. Vieira, Z. Najmudin, R. Bingham, C. Joshi, and T. Katsouleas, *Plasma Phys. Controlled Fusion* **56**, 084015 (2014).

<sup>25</sup>B. R. Maddox, H. S. Park, B. A. Remington, N. Izumi, S. Chen, C. Chen, G. Kimminau, Z. Ali, M. J. Haugh, and Q. Ma, *Rev. Sci. Instrum.* **82**, 023111 (2011).

<sup>26</sup>T. Bonnet and M. Comet, *Rev. Sci. Instrum.* **84**, 103510 (2013).

<sup>27</sup>P. A. Ross, *J. Opt. Soc. Am.* **16**, 433 (1928).

<sup>28</sup>F. Albert, B. B. Pollock, J. L. Shaw, K. A. Marsh, J. E. Ralph, Y.-H. Chen, D. Alessi, A. Pak, C. E. Clayton, S. H. Glenzer, and C. Joshi, *Phys. Rev. Lett.* **111**, 235004 (2013).